JOM, Vol. 65, No. 9, 2013
DOI: 10.1007/s11837-013-0700-6
© 2013 The Author(s). This article is published with open access at Springerlink.com

Features of Transmission EBSD and its Application

SEIICHI SUZUKI[1,2]

1.—TSL Solutions KK, #SIC2-401, 5-4-30, Nishihashimoto, Midori-Ku, Kanagawa, Sagamihara 252-0131, Japan. 2.—e-mail: info@tsljapan.com

Features of transmission electron backscatter diffraction (EBSD) observation with a standard EBSD (*s*-EBSD) detector are surveyed in this study. Heavily deformed Al and 8Cr tempered martensite transmission electron microscope (TEM) specimens were used for this study. It is shown that a specimen tilt angle of ~30°–40° in the opposite direction of the usual 70° and a smaller working distance in the range 4 mm–5 mm are recommended when using a *s*-EBSD detector. Specimen thickness and accelerating voltage (Acc.V) have a strong affect on the quality of transmission EBSD patterns and orientation maps. Higher Acc.Vs are generally recommended to get good quality orientation maps. In case of very thin specimens, lowering the Acc.Vs will give better results. In the observation of a thin film of an 8Cr tempered martensite steel specimen, it is confirmed that *t*-EBSD can provide images and detailed quantitative orientation data comparable with that obtained by TEM. It is also shown that small precipitates of $Cr_{23}C_6$ with sizes around 30 nm could be detected and their orientations measured.

INTRODUCTION

The transmission electron microscope (TEM) is generally considered the tool of choice for the microstructural analysis of materials at the nanoscale. Atomic scale resolution is becoming routine for modern high-resolution TEMs. Electron diffraction can be used to analyze the crystal structure and crystallographic orientation on a point-by-point basis in the TEM. Spot diffraction, Kikuchi diffraction, and convergent beam diffraction are all viable techniques for performing such analysis. However, one of the major difficulties that remains is the mapping of orientations in an automated and robust manner. Such capabilities are beginning to emerge using automated indexing for spot diffraction patterns. Combining these automated indexing techniques with the nanobeam diffraction capability of the TEM, the spatial resolution of orientation mapping in the TEM can reach a 2 nm to 3 nm scale.[1] But the accuracy of measured orientations is still limited compared with the results of electron backscatter diffraction (EBSD) in the scanning electron microscope (SEM). The achievable spatial resolution of standard EBSD (*s*-EBSD) is still at the 20 nm–30 nm level when combined with field emission SEM, although its orientation accuracy is stable and it is generally a range of 0.5°. The automated EBSD technique has made it nearly routine to quantitatively analyze the microstructure of materials available based on crystallographic orientation. However, achieving spatial resolutions better than 20 nm–30 nm with EBSD continues to be difficult even with the most modern EBSD systems and SEMs. A great advance would be to marry the routine quantitative capability of automated EBSD with the spatial resolution of the TEM—to be able to achieve EBSD spatial resolutions measured in the nm instead of in the tens of nm of *s*-EBSD.[1]

In 2012, Keller and Geiss demonstrated that EBSD patterns could be acquired from a thin film specimen by transmitted electrons in the SEM.[2] They used a *s*-EBSD detector mounted on their SEM and a thin film specimen (TEM specimen) was tilted in the opposite direction of the standard reflection EBSD configuration to enable a geometry where a transmitted electron can hit the phosphor screen of the EBSD detector in the standard position as shown in Fig. 1. They showed that EBSD patterns formed by these transmitted electrons came from very small volumes of the specimen. They suggested that this technique could improve that spatial resolution of EBSD. Following their paper, Trimby showed that this high-resolution

(Published online July 27, 2013)

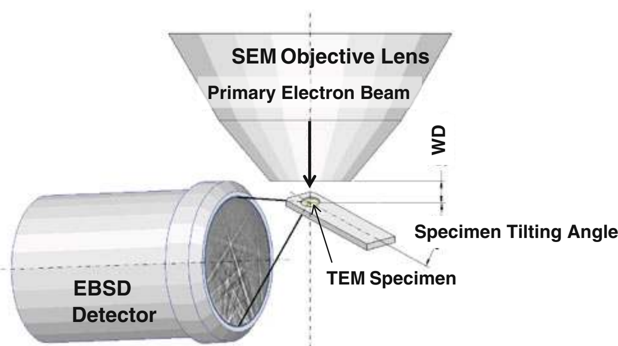

Fig. 1. TEM specimen setting arrangement for *t*-EBSD.

EBSD image can be acquired by using this technique.[3] In this paper, the basic features of the EBSD patterns formed by transmitted electrons are surveyed, and an application of the technique to analyze the microstructure of a 8Cr tempered martensite specimen is described.

Keller and Geiss termed this technique "transmission EBSD (*t*-EBSD)." There are some arguments about whether it is correct to refer to this technique as *t*-EBSD. The term "backscatter" is not truly valid. Therefore, the term "transmission Kikuchi diffraction" is suggested instead. However, since the name of EBSD is already recognized widely as a method for analyzing microstructure using Kikuchi electron diffraction patterns in the SEM, the term of *t*-EBSD is also used in this articles out of respect for the initial work of Keller and Geiss.

EXPERIMENTS

The effects of specimen tilt angle, working distance (WD), and accelerating voltage (Acc.V) were studied to determine the optimal conditions for *t*-EBSD. All *t*-EBSD patterns and map data were obtained by use of a JEOL JSM-7001F SEM (JEOL Ltd., Akishima, Tokyo, Japan) with EDAX-TSL OIM EBSD system (EDAX Inc. (Ametek), Mahwah, NJ) equipped with a DigiView 1612 high-speed charge-coupled device camera. Special specimen holders were made to set the specimen at tilt angles of 20°, 40°, and 60° from the horizontal plane in a direction opposite to the *s*-EBSD tilt direction as shown in Fig. 1. An examination of the effects of WD and the Acc.V were tested by varying the WD to values of 5 mm, 10 mm, and 15 mm and Acc.V of 15 kV and 25 kV. A capture angle of *s*-EBSD patterns at a 15-mm WD is ~75° with this geometry. The capture angle varies depending on WD and becomes about 65° at a 5-mm WD. A thin film specimen of annealed Al after heavy deformation and a thin film sample of 8Cr tempered martensite steel were used for these experiments. These specimens were prepared originally for TEM observation by electro-chemical etching, which has a hole near the center of the specimen. The sample thickness around the hole is thin, and it becomes thicker away from the hole.

RESULTS

Heavily Deformed Al Thin Film

Effects of Specimen Tilt Angle and WD

The effects of specimen tilt angle and WD on *t*-EBSD patterns with these experimental settings are shown in Fig. 2. These patterns were collected from the same position of the specimen under a specified condition. A portion of the pattern is obscured when the specimen at a lower tilt angle is used along with a longer WD. These results suggest that a shorter WD and higher tilt angle are better for acquiring *t*-EBSD patterns for this specific EBSD detector geometry. Figure 3 shows inverse pole figure (IPF) orientation maps overlaid on image quality (IQ) maps (top half) and IQ maps (Sidebottom half) obtained at different specimen tilt angles by *t*-EBSD from the Al specimen. IPF maps are maps colored according to the crystal plane normal direction (ND) aligned with a specified sample direction (in this case the sample normal). The color scheme used has red for (001), green for (101), and red for (111). This scanned area is thick at the left side and becomes thinner at the right. The WD was set at 5 mm based on the results of Fig. 2. The sharpness of the IQ maps became better at lower tilt angles (20°). This is more apparent in the thicker area on the left-hand side of the maps. This can be explained by the fact that the electron beam path in the specimen becomes longer with increased tilt of the specimen. This results in increasing beam spreading in the specimen leading to poor spatial resolution. Thus, the spatial resolution will be better with decreasing specimen tilt. On the other hand, IPF orientation maps look better with higher tilt. The average Confidence Index that shows the reliability of indexing results had 0.08, 0.14, and 0.31 for the IPF maps with a tilting angle of 20°, 40°, and 60°, respectively. As shown in Fig. 2, the contrast of bands at the upper part of the detector becomes very weak with decreasing tilt. It becomes difficult for the automated band detection of the bands to correctly detect bands from this area of the *t*-EBSD pattern resulting in poor indexing.

Effects of Specimen Thickness

The quality of *t*-EBSD patterns is very much dependent on the thickness of the specimen. This dependence also has a strong effect on the spatial resolution of the *t*-EBSD map. Figure 4 shows examples of how the pattern changes with specimen thickness. The specimen is 8Cr tempered martensite, and one grain occupies the full thickness of the sample. These patterns are acquired at 25 kV. It shows that if the specimen is very thin, the pattern becomes weak and noisy as shown in Fig. 4a. As the specimen becomes thicker, the patterns start to lose their sharpness starting at the outer edges of the screen as shown in Fig. 4c and d. Then as the

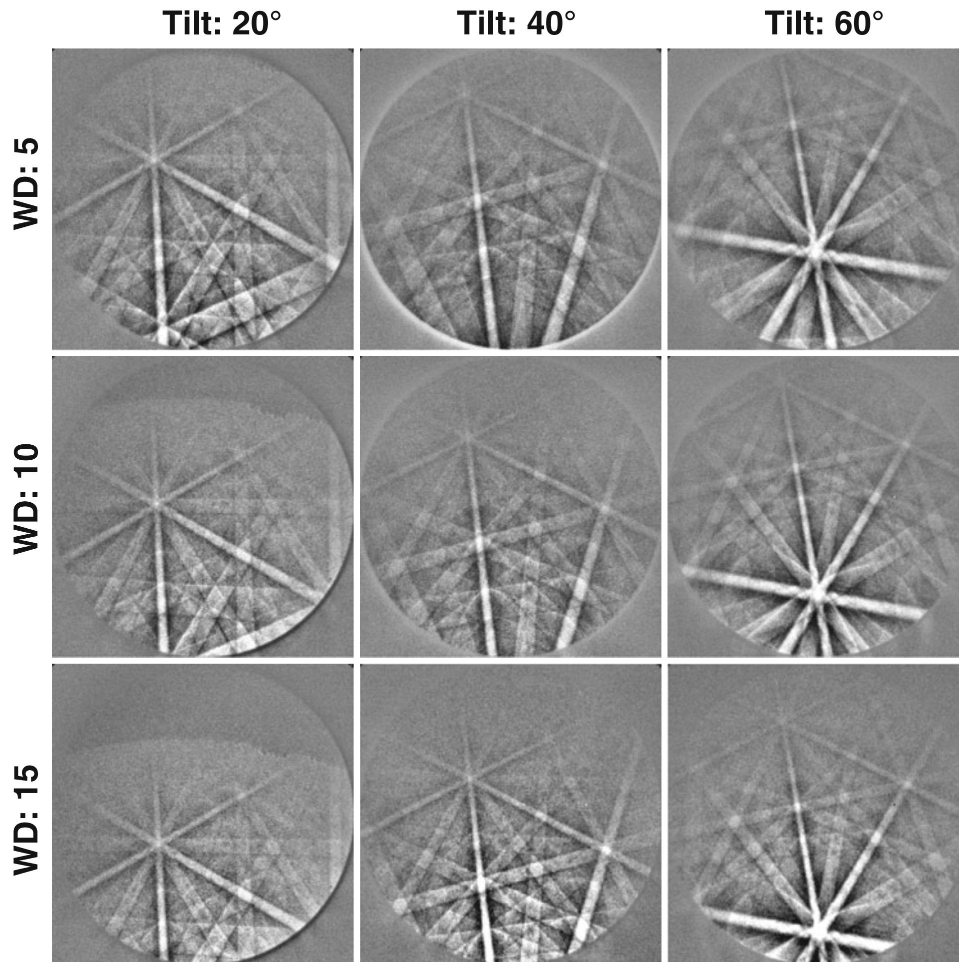

Fig. 2. Changes in *t*-EBSD patterns depending on specimen tilting angle and WD. Specimen was Al thin film, and Acc.V was set at 25 kV.

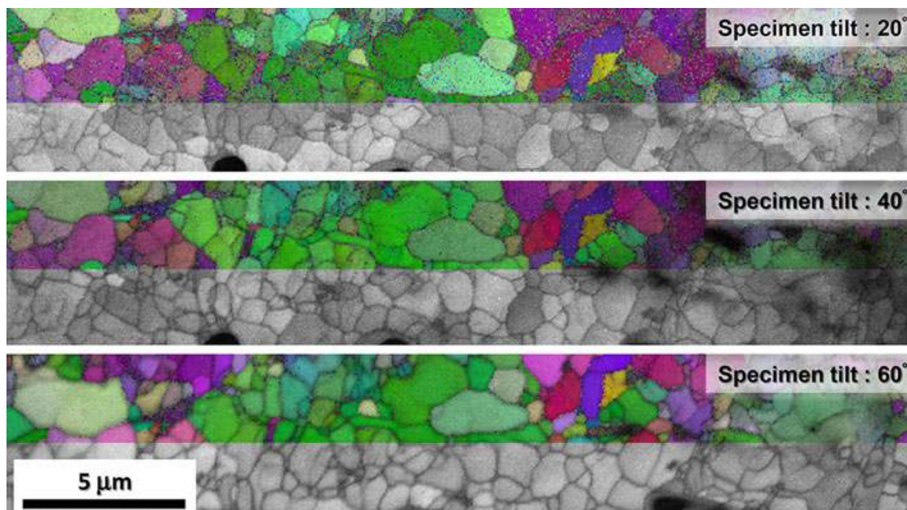

Fig. 3. Effects of specimen tilting angle to *t*-EBSD maps. Spatial resolutions is better in lower tilting angle, but indexing result is better in higher tilting angle.

sample becomes thicker, the band contrast reverses as shown in Fig. 4f.[4] It should be noted that all of these patterns can be indexed by the computer algorithms, but it is easy to understand that the algorithms will struggle to achieve high-precision orientation measurements especially for

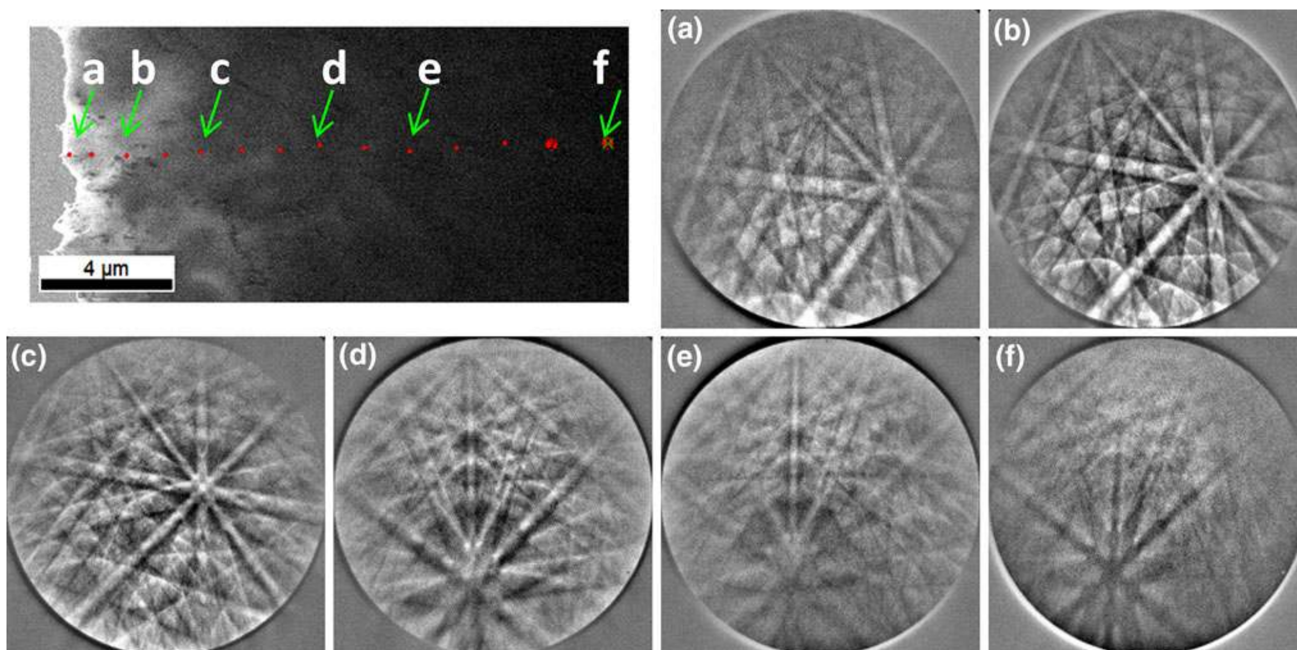

Fig. 4. Example of how pattern changes depending on specimen thickness. These patterns are acquired at the position shown above of 8Cr tempered martensite specimen. Position (*a*) is very close to the edge of the hole.

the patterns within the thicker region of the sample. Figure 5 shows *t*-EBSD IPF orientation maps of the Al specimen near the hole at Acc.V of 15 kV and 25 kV. The specimen thickness is thin at the left-hand side and becomes thicker at the right-hand side of the maps. The sharpness of the maps obtained from the thicker regions of the sample (right sides of the maps) are obviously better in the map obtained at 25 kV than that obtained at 15 kV. But the quality of the left side of the map (corresponding to the thin region of the sample) obtained at 15 kV is obviously better than that obtained at 25 kV. The quality of the map data clearly depends on both specimen thickness and Acc.V. The thicker the sample, the higher Acc.V that should be used to achieve good *t*-EBSD results.

Next, the effect of overlapping grains through the thickness of the sample was investigated. If the specimen thickness stays within a reasonable range (estimated as 100 nm to 400 nm) for *t*-EBSD, overlaid grains do not appear to seriously hamper the formation of *t*-EBSD patterns. Figure 6 compares IPF maps overlaid on IQ maps acquired by both *s*-EBSD and *t*-EBSD. Once again, the specimen is the heavily deformed Al thin film and the observation area was set near the hole. Figure 6a and b are maps acquired by *s*-EBSD from the front and back surfaces of the same area of the specimen, respectively. The back surface map is reversed left to right for comparison with the front surface map. The grains highlighted by blue arrows are examples of grains extending through the full thickness of the sample. Note that the maps are similar for the thin regions of the sample area near the edge of the hole (near left bottom corner), whereas regions of the map from the thick parts of the sample (near the top and right) are very different. The dissimilarity of the maps in the thick regions is due to grains that overlap in the thickness direction of the sample. Figure 6c is an orientation map acquired by *t*-EBSD from the same area of the specimen. This *t*-EBSD image was acquired directing the electron beam on to the front surface of the sample. The IPF maps Fig. 6b and c are very similar. This shows that *t*-EBSD patterns are primarily formed at the bottom (or exiting) surface layer of the specimen. This is fortunate, as grains that overlap in the thickness direction do not detrimentally affect the formation of *t*-EBSD patterns as long as the total thickness of the specimen stays within a reasonable range for transmission. The lower part of the *t*-EBSD map shown in Fig. 6c is particularly good, but it becomes noisier at the upper right, which is the thicker part of the specimen.

Cr Tempered Martensite

TEM Bright Field versus t-EBSD IQ Map

Figure 7shows the microstructure of tempered martensite of 8Cr steel for the same area observed by both TEM and *t*-EBSD. Figure 7a is a bright field image obtained by TEM at 200 kV. The magnification was set at 15 kx. Figure 7b is an IQ map obtained by *t*-EBSD in the SEM at 25 kV at a magnification of 10 kx. Figure 7c is an IQ map obtained by *s*-EBSD in the SEM at 15 kV. Figure 7d is a SEM image obtained by SEM at 25 kV. The images of Fig. 7b–d were obtained at tilt condition,

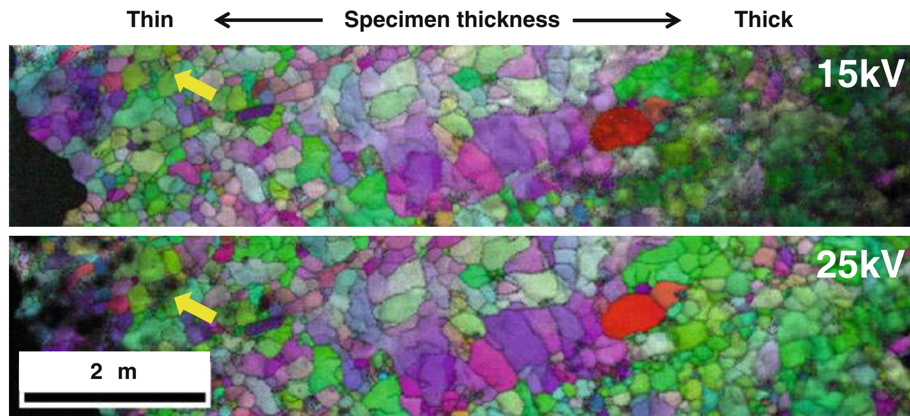

Fig. 5. Effects of specimen thickness and Acc.V on the quality of *t*-EBSD maps. IPF maps overlaid on IQ map acquired at Acc.V of 15 and 25 kV with Al thin film specimen. Yellow arrows show the same part of the specimen at a thin area.

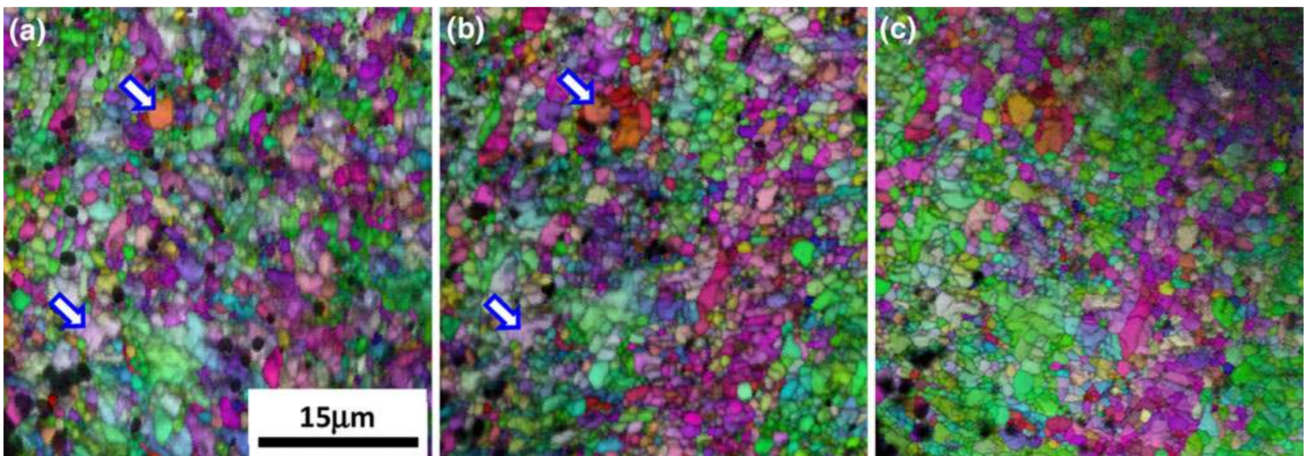

Fig. 6. The comparison of IPF maps overlaid on IQ maps acquired by *s*-EBSD and *t*-EBSD. (a) and (b) are images of *s*-EBSD acquired from front surface and back surface of same area, respectively. White arrows show same grains. (c) is also an IPF map acquired by *t*-EBSD from the same area of the specimen. It was acquired illuminating electron beam to the front surface and getting *t*-EBSD patterns from the back surface.

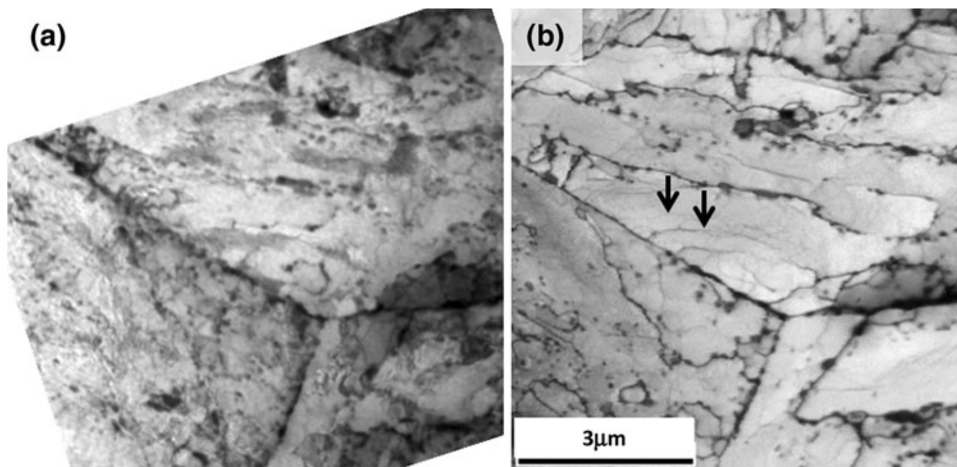

Fig. 7. (a) is a bright field image obtained by TEM at 200 kV, and (b) is an IQ map obtained by *t*-EBSD at 25 kV. The specimen was a thin film of tempered martensite of 8Cr steel.

and these are tilt-corrected images. These images are from the exact same area, and Fig. 7a and b, as well as Fig. 7c and d, look relatively similar, respectively, even though the mechanism of image formation is completely different.

TEM bright field images exhibit a diffraction contrast image formed by elections penetrating through the specimen. The specimen shows a lot of small orientation changes in the field of view making the contrast of the bright field image appear quite complex.

The IQ map by EBSD is created using the sum of intensities of the bands in the EBSD patterns as determined by the band detection computer algorithm (Hough transform[5]). The contrast in the IQ map reflects the sharpness of the bands in the individual EBSD patterns obtained at each point in the map. If there is no damage by specimen preparation, contamination, or oxides formed on the surface of the specimen, the IQ map shows the quality of the crystal of the specimen. The sharpness of EBSD is reflective of the degree of disorder of the crystal in the diffracting volume. Grain boundaries can be considered regions where the atoms in the crystal lattice are highly disordered. The differences in the IQ maps in Fig. 7b and c arise from the difference in the diffracted electrons, transmitted versus backscattered electrons, and the specimen tilt angle. The *t*-EBSD patterns used in constructing this IQ map are formed by diffracted electrons transmitted through crystals at the bottom layer of the specimen. They are not the results of information integrated in the thickness direction. Thus, the IQ map appears less complicated relative to the TEM bright field image. The *s*-EBSD patterns used for the IQ map are formed by diffracted electrons scattered in the backward direction. The sample needs to be tilted more to acquire these backscattered electrons effectively. This actually causes larger beam spreading in the specimen resulting in poor spatial resolution.[3] It is also affected more by sample surface topography than *t*-EBSD. The SEM image mainly reflects the surface topography of the specimen, which is why the images of Fig. 7c and d look relatively similar.

One question that arises in an inspection of these results is whether the fine and faint lines observed within the grains in the IQ map as highlighted by red and blue arrows in Fig. 7b are dislocations. The misorientations between both sides of the clearer lines shown by black arrow as an example are 4°–5° or more, and they are small angle boundaries. The misorientations between both sides of these fine and faint lines highlighted by the red arrow are generally $<1°$, or within the fluctuation of orientation measurement. The misorientations between a little bit thicker lines highlighted by the blue arrow are a little bit larger. Given the magnification used in these images, it is difficult to imagine a source for these very fine lines except dislocations. Dislocations disorder the crystal lattice and thus affect the pattern quality leading to darker points in the IQ map. Thus, it can be thought that very fine lines are potentially individual dislocations and the slightly thicker lines having slightly larger misorientations indicate a tangle of dislocations or the presence of a dislocation wall. However, this has not been confirmed in this experiment.

Orientation Analysis

Figure 8 shows an IPF orientation map from the martensite structure obtained by *t*-EBSD. Detailed orientation information can be gleaned from the quantitative data from which these maps are reconstructed. The small changes in color between the areas labeled as A, B, C, and D in the IPF map correspond to small differences in orientation as is evident in the unit cell overlays in Fig. 8a. There are about 6°–7° differences between points A and C, as well as B and D, and 1°–2° differences between A and C, as well as B and D. These misorientations correspond to orientation relations between variants in the martensite transformation.[6,7]

Figure 9 a shows a (001) pole figure from the orientation data obtained from the observed area. The orientation data were rotated to bring the orientation cluster marked by the red circle to the center of the pole figure. The rotation about the ND was also adjusted. After these rotations, the orientations of upper side grains were highlighted and plotted in the (001) pole figure as shown in Fig. 9c using the same coloring as in the map. The pole figure shows the part of martensite variant orientation relations. Then two small spots shown by blue and light blue color arrows are two spots that were part of eight spots that would be created around the (001) pole of prior austenite after martensite transformation. The blue and light blue colors in the map of Fig. 9b are highlighted again by using these two variant spot in the pole figure of Fig. 9c. It shows clearly the orientation relations explained in the previous paragraph regarding Fig. 8a.

Figure 10 shows the distribution of misorientations for the map data. The colored ranges of the chart are highlighted on the IQ map. Blue boundaries correspond to general boundaries or twin boundaries of the original austenite phase before martensite transformation. Green boundaries highlight the boundaries between matrix and chromium carbide. Yellow boundaries indicate variant orientation relations for the martensite transformation. Red boundaries show the boundaries with the twin orientation relation.

All these analyses based on orientation maps, which are not practically available with TEM observation, can be done now relatively easily by *t*-EBSD.

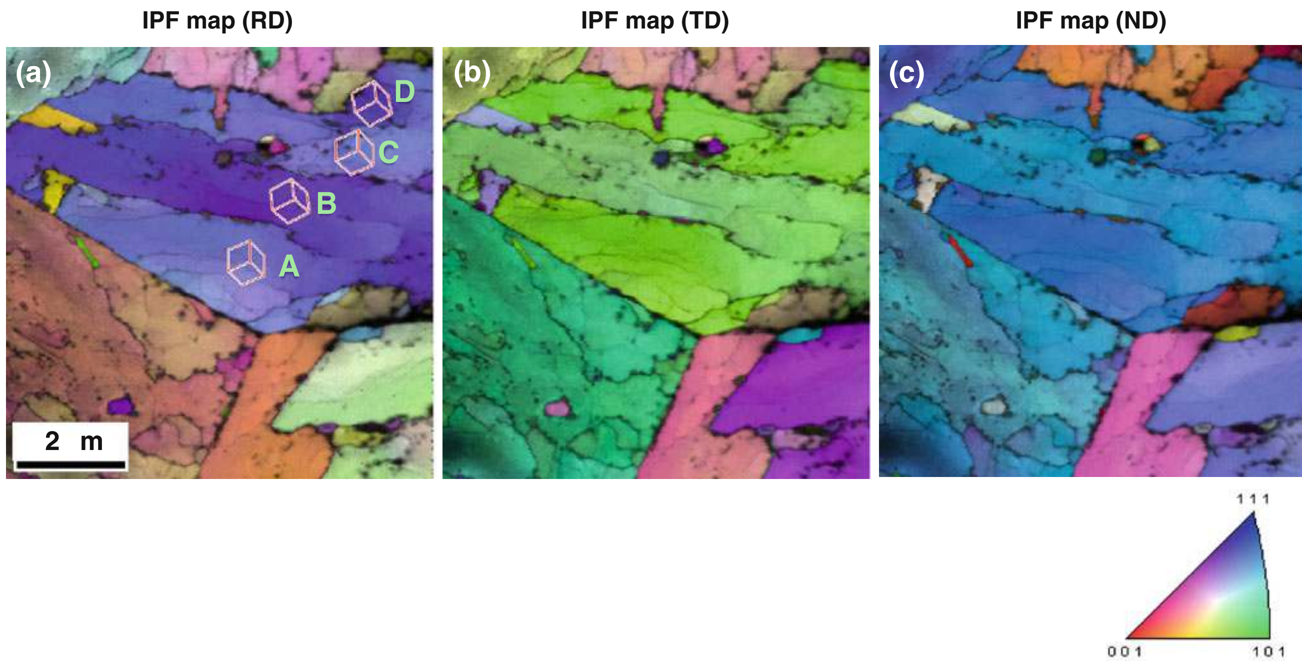

Fig. 8. IPF orientation maps of RD, TD, and ND sample directions.

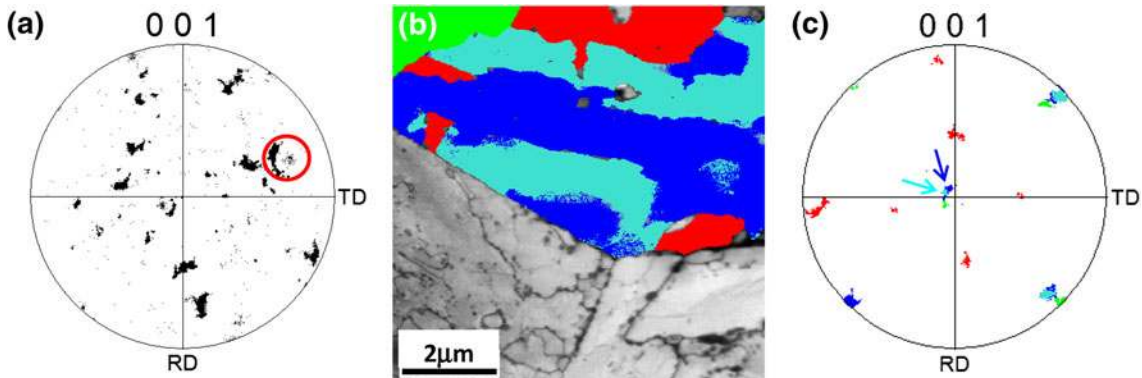

Fig. 9. (a) is a (001) pole figure of the whole scan area. (c) is a pole figure of selected area colored in map (b) after rotating the orientation data to bring the cluster marked by a red circle to the center and rotation around the ND axis is adjusted.

Analysis of Chromium Carbide Precipitates

Figure 11 shows an IPF map and an IQ map from different areas of the same specimen. Small grains highlighted in green on the IQ map are chromium carbides ($Cr_{23}C_6$) that have a cubic structure. These data were taken with a step size of 10 nm at an Acc.V of 25 kV. The magnification was set at 15 kx. The minimum size of chromium carbide that was detected reasonably well was about 30 nm in diameter. However, the ability to count these small precipitates will depend on where those precipitates are located. If they are located on the back surface, they will produce clear patterns. If they are on the inside of the specimen, the patterns will be noisy or completely missing. Figure 12 shows examples of *t*-EBSD patterns taken from the chromium carbide precipitates and the ferrite matrix. Both of these two phases have a cubic crystal structure with different structure factors. They were easily differentiated from each other. Chromium carbides are precipitated along small angle grain boundaries, and most of them have the same orientation, although they were precipitated separately. An example of the orientation relation between the ferrite matrix and the chromium carbide precipitates is shown in the (001) pole figure in Fig. 11c. The two unit cells show the orientation of ferrite matrix and carbide precipitate, respectively. This is a typical example of misorientation between chromium carbide and ferrite matrix, that is, a 45° rotation around a near <001> axis with either side of the ferrite matrix. The common rotation axis is

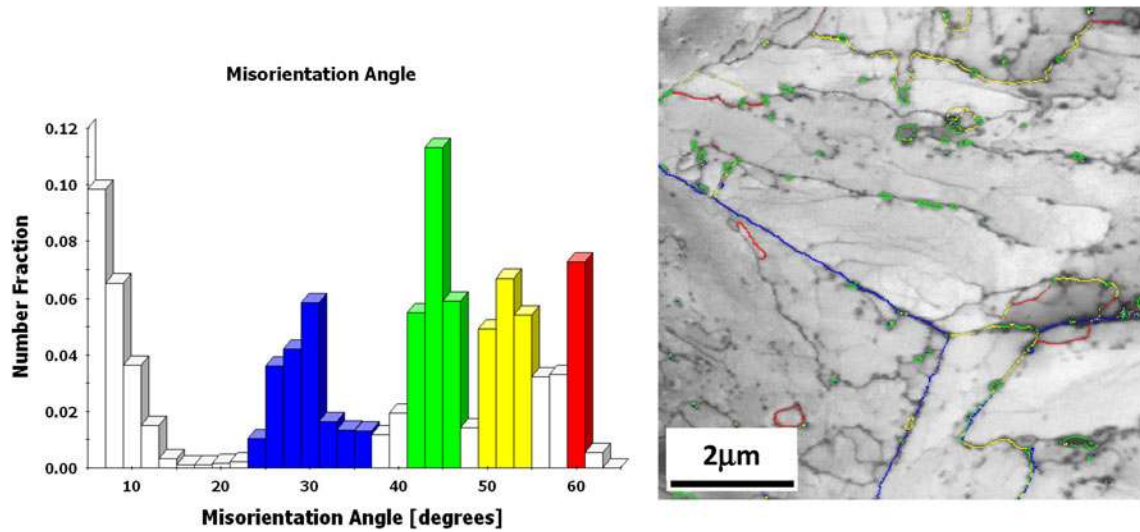

Fig. 10. Misorientation chart of orientation map data. The colored range of the chart is highlighted on the IQ map. The boundaries of these misorientation angles show some specific features.

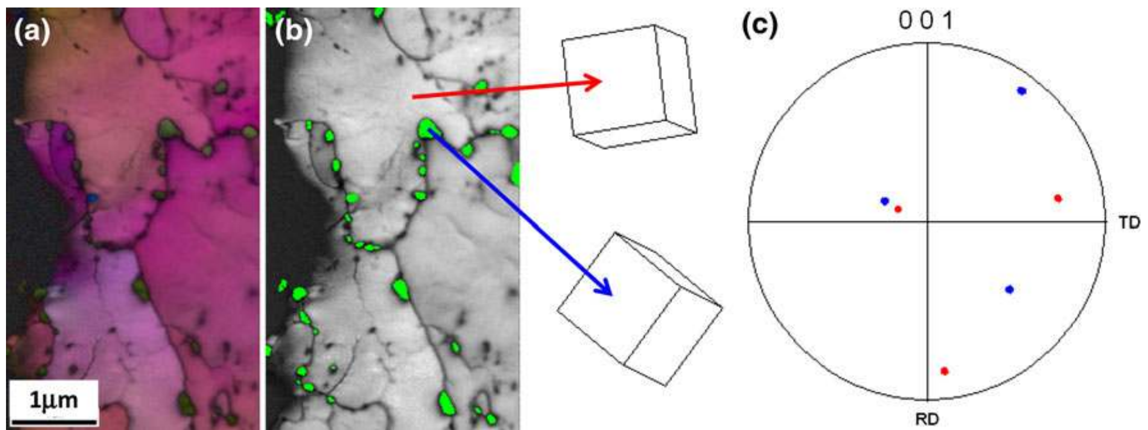

Fig. 11. (a) IPF map overlaid on IQ map, and (b) IQ map where chromium carbides are highlighted with a green color. (001) Pole figure that shows typical misorientation relation between chromium carbides and ferrite matrix.

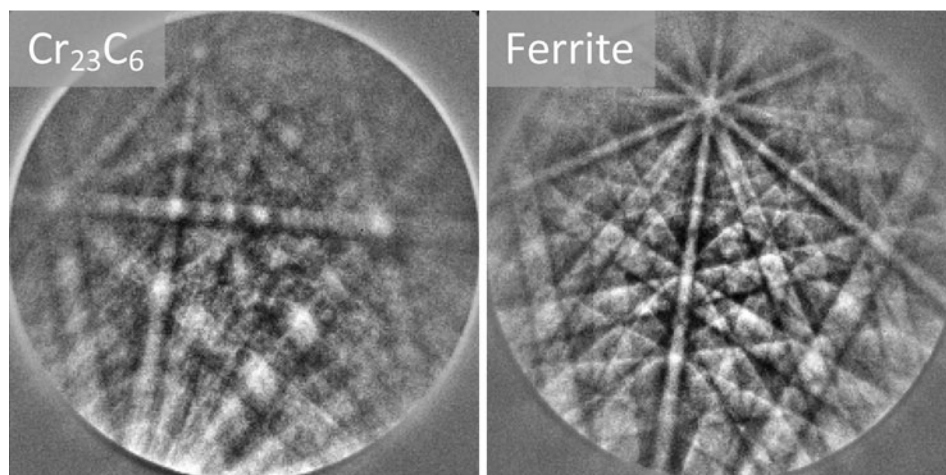

Fig. 12. Examples of *t*-EBSD patterns from chromium carbide and ferrite matrix.

near <001>, but it is always tilted from exact <001> by about 9°.

SUMMARY

Specimen Tilt Angle and WD

It is concluded that the optimum specimen tilt angle for *t*-EBSD with the system used for these experiments is to be ~40°. Figure 3 shows that a smaller tilt angle gives better spatial resolution results. A higher tilt angle increases the practical specimen thickness for electron beam travel vertically in the specimen. However, lower indexing results are obtained at decreasing specimen tilt due to the loss of information at the upper part of the phosphor screen. This is due to the EBSD detector position, which is relatively high with respect to the specimen position. It is very opportune that an *s*-EBSD detector can be used for *t*-EBSD data collection without any modification. However, the typical *s*-EBSD position is not the ideal detector position for *t*-EBSD. If the detector can be set at a lower position with a higher elevation angle, a smaller specimen tilt angle can be used that would improve the quality of *t*-EBSD patterns and the spatial resolution.

Specimen Thickness

Specimen thickness has a significant effect on the quality of *t*-EBSD patterns; hence, it also strongly affects the collection of the *t*-EBSD orientation map data as Trimby discussed in his paper.[3] One feature of the *t*-EBSD pattern is that band contrast becomes inverted if electrons are diffracted from a thicker part of the sample with the same lattice orientation, namely, a single though-thickness grain or a large grain. This can be explained by the travel length of diffracted electrons along some crystal planes. The bands in EBSD patterns are projections of crystal planes within the diffracting crystal lattice. If diffracted electrons travel longer distance along the crystal plane, they are scattered by atoms existing along the electron travel direction. As a result, the number of electrons traveling in the original diffracted direction decreases considerably leading to a loss of intensity. Thus, the contrast becomes inverted. Present EBSD software is programmed to detect bright peaks in the Hough transform used for automated band detection, and thus, these inverted contrast bands will not be correctly detected resulting in poor indexing. This also depends on Acc.V; when a higher Acc.V is used, the inverted contrast is minimized. However, the quality of the results from the thinner areas of the sample will diminish. This means a balance between the specimen thickness and Acc.V must be achieved to obtain good *t*-EBSD results.

Overlapping Grains

The observations made in this study show that overlapping grains do not pose a particular problem to *t*-EBSD. This is a big advantage over TEM-based approaches to the collection of orientation data where overlapping grains can lead to ambiguous results. Diffraction patterns from *t*-EBSD are formed only from the bottom surface (exiting surface) of the sample. Grains that are bigger and extend through the thickness of the sample are actually more problematic for *t*-EBSD as they can produce patterns with an inversion in the band contrast.

Spatial Resolution

There is still some discussion regarding the spatial resolution of the *t*-EBSD method. It is clear from the results presented in this work that the spatial resolution depends very much on specimen thickness and Acc.V. It is assumed that the resolution depends on probe size too. Grain boundaries tend to appear more clearly than in *s*-EBSD maps as far as the specimen thickness is in a reasonable range. But the clarity still depends on the inclination of the grain boundary relative to the surface plane. Assuming optimal conditions for both *t*-EBSD and *s*-EBSD, *t*-EBSD is capable of spatial resolutions on the order of the probe size, which is considerably better than *s*-EBSD.

CONCLUSIONS

Specimen thickness and Acc.V have a strong affect on the quality of *t*-EBSD patterns and orientation maps. Higher Acc.Vs are generally recommended to get good quality orientation maps. In case of the very thin specimens, lowering Acc.V will give better results. A spatial resolution of the 10-nm level can be achieved by *t*-EBSD, but it depends on specimen thickness and Acc.V.

An existing EBSD detector can be used for *t*-EBSD. However, a specimen holder that allows for transmission of the electron beam is required. When using a *s*-EBSD detector, it is recommended that a specimen tilt angle of ~30° to 40° in the opposite direction of the usual 70° be used. A smaller WD should also be used: in the range 4 mm–5 mm.

In this study, a thin film of an 8Cr tempered martensite steel specimen was observed by *t*-EBSD. It is confirmed that *t*-EBSD provides images and detailed quantitative orientation data comparable with that obtained by TEM. A study of small precipitates of $Cr_{23}C_6$ was also undertaken. Precipitates with sizes around 30 nm could be detected and their orientations measured. It was shown that $Cr_{23}C_6$ precipitations appeared along small angle boundaries with strong orientation relations to the ferrite matrix. Very fine lines were observed in IQ

images of 8Cr tempered martensite steel specimen, which were acquired with very small step sizes such as 20 nm or less. These fine lines are thought to be dislocations, or arrays or tangles of dislocations, but this has not been confirmed in this experiment.

ACKNOWLEDGMENTS

The author expresses his appreciation to Dr. Hiroki Tanaka of Sumitomo Light Metal Industry KK and Prof. Soumei Ohnuki and Mr. Tomoki Kubota of Hokkaido University for providing TEM specimen for this research work. The author also expresses his appreciation to Dr. Stuart Wright of AMETEK/EDAX division for very fruitful discussions to complete this article. Furthermore, the author acknowledges the Japan Institute of Metals and Materials for granting use of the data of Figs. 1, 5, 6, and 7, which were originally used in the author's article to be published in *Journal of Japan Inst. Metals* 7, 2013.

OPEN ACCESS

This article is distributed under the terms of the Creative Commons Attribution License which permits any use, distribution, and reproduction in any medium, provided the original author(s) and the source are credited.

REFERENCES

1. P. Moeck, S. Rouvimov, E.F. Rauch, M. Veron, H. Kirmse, I. Hausler, W. Neumann, D. Bultreys, Y. Maniette, and S. Nicolopoulos, *Cryst. Res. Technol.* 46, 589 (2011).
2. R.R. Keller and R.H. Geiss, *J. Microsc.* 245, 245 (2012).
3. P.W. Trimby, *Ultramicroscopy* 120, 16 (2012).
4. A. Winkelmann and G. Nolze, *Ultramicroscopy* 110, 190 (2010).
5. N.C. Krieger Lassen, K. Conradsen, and D.J. Jensen, *Scanning Microsc.* 6, 115 (1992).
6. A.-F. Gourgues, H.M. Flower, and T.C. Lindley, *Mater. Sci. Technol.* 16, 26 (2000).
7. N. Takayama, G. Miyamoto, and T. Furuhara, *Acta Mater.* 60, 2387 (2012).